ASPECT SENSITIVITY OF EQUATORIAL F-REGION IONOSPHERIC IRREGULARITIES

A Thesis

Presented to the Faculty of the Graduate School

of Cornell University

in Partial Fulfillment of the Requirements for the Degree of

Master of Science

by

Russell Blain Hedden

May 2010

ABSTRACT

The small-scale irregularities of equatorial spread-F (ESF) are highly aligned with the geomagnetic field. Aspect angles (rms deviations from perfect alignment) have been found to be routinely less than .01°. Measuring angles this small requires the use of radar interferometry because the angles being measured are much smaller than the beamwidth of any incoherent scatter radar. The technique used to measure the aspect angles along with data collected in March, 2009 at the Jicamarca Radio Observatory are presented.

BIOGRAPHICAL SKETCH

Russell Blain Hedden was raised in Clemson, South Carolina where he attended D.W. Daniel High School. While a student at Clemson University, Russell studied physics and graduated magna cum laude with general and departmental honors with a Bachelors of Science in Physics in 2008.

This thesis is dedicated to my love, Kristen Purvis.

ACKNOWLEDGEMENTS

Fist I would like to thank my advisor, Dr. David Hysell, without whom this thesis would not be possible. I would also like to thank Dr. Michael Kelley for his guidance and support during my studies. Also, thank you to the entire staff at Jicamarca Observatory which provided the data upon which this thesis is based. Finally, I am in debt to Dr. John Meriwether for showing me the joys of aeronomy and his support and encouragement throughout my undergraduate and graduate education.

TABLE OF CONTENTS

LIST OF TABLES

LIST OF FIGURES

CHAPTER 1

INTRODUCTION

Equatorial spread-F (ESF) is a phenomenon characterized by plasma irregularities in the equatorial F-region of the ionosphere. There are four processes which may contribute to the creation of the plasma irregularities. At scales larger than 200 km, gravity wave seeding and electrodynamic uplift are the main influence. For scales between a few tens of kilometers to 200 km, shear effects may contribute to the ESF. The generalized Rayleigh-Taylor instability occurs at scales between 100 m and 20 km, and at the smallest scales (1 m - 100 m), diffusive dampening via wave-wave coupling to damped waves likely contributes (*Kelley*, 2009).

Equatorial spread-F primarily occurs at night, although it occasionally occurs during the day. It has two main forms, bottomside and topside. Both types of ESF drift eastward under the control of the F-region dynamo. Bottomside irregularities occur generally below 400 km and last for extended periods of time. Topside irregularities, or plumes, generally are only seen at a radar site sporadically and can reach altitudes above 800 km. Neither form of ESF occurs every evening, and determining which nights ESF will occur at a given location is an area of active research.

The first observations of ESF were made in the 1930s with ionosondes. The name ”equatorial spread-F” is derived from the spread in range or frequency of the reflected ionosonde signal (*Berkner and Wells*, 1934). Little progress was made into the understanding of ESF until the 1960s with construction of HF and VHF radars in the equatorial region, particularly the 50 MHz Jicamarca radar in Peru. *Farley et al.* (1970) published a review of the current theories explaining ESF and determined that none were correct. Over the next four

decades, considerable progress has been made in both the theoretical and experimental understanding of ESF.

Both bottomside and topside ESF are highly aligned with the geomagnetic field. Therefore, only when a radar beam is pointing nearly perpendicular to the geomagnetic field will echoes be received. The aspect angle of the echoes is the angle from the perpendicular direction over which echoes are received. Determining exactly how aligned the echoes are is not trivial due to the aspect angle being, at most, only a few percent of a degree. The beamwidth of radars such as Jicamarca is meanwhile a degree or more. Nonetheless, precisely determining the aspect angle is important for providing experimental validation for theories.

Measuring the small aspect angles of ESF is possible due to the radar interferometry technique developed by *Farley et al.* (1981). The technique allows for the measurement of root-mean-square (RMS) aspect widths much smaller than the radar beamwidth. In 1985, using north-south aligned baselines, the first aspect sensitivity experiments using the interferometry technique were performed (*Kudeki and Farley*, 1989).

The radar interferometry method was later applied to ESF by *Farley and Hysell* (1996) and *Hysell and Farley* (1996). The observations provided important insights into mechanisms driving ESF plasma instabilities. No equatorial F-region aspect sensitivity measurements have been made since 1993. Since 1993, the Jicamarca radar has been upgraded with the introduction of digital receivers. Due to the limitations of analog receiver technology, the previous aspect sensitivity measurements were only able to establish an upper limit on the aspect width of ESF echoes. Our goal is to use the improved technology at the Jicamarca radar to validate and improve upon the results of the earlier

studies.

The *Hysell and Farley* (1996) paper concluded the small aspect angles observed in the equatorial F-region constitute evidence that nonlinear mode coupling is required to explain the irregularities in ESF. In particular, highly nonlocal three-wave interactions are causing the irregularities. The decay of the irregularities is caused by parallel and perpendicular diffusion, and the irregularities with the largest parallel wavenumbers decay most rapidly. Therefore, the more field-aligned structures linger as time progresses, and the aspect angle decreases with time as the irregularities dissipate. *Hysell and Farley* (1996) proposed the radar observations represent an average over the lifetime of the irregularities.

The aspect angle of the irregularities seems to be independent of most geophysical parameters. The theory developed in *Hysell and Farley* (1996) shows the aspect angle scaling like $\sqrt{\nu_{ei}}$, where ν_{ei} is the electron-ion collision frequency. However, when ion-neutral and electron-neutral collisions begin to dominate electron-ion collisions, the aspect width should begin to increase.

Improvements in technology since the work of *Farley and Hysell* (1996) and *Hysell and Farley* (1996) allow for increased sampling in range and time. Thus, in the current study, we examine the data in to attempt to determine if the theory above is sufficient to explain any variation seen in aspect angles.

The thesis is organized as follows. In Chapter 2 the Jicamarca Radio Observatory is introduced, the experimental design for the aspect sensitivity measurements is presented, and the theory behind the aspect sensitivity measurement technique is developed. Chapter 3 presents the experimental results. Chapter 4 presents our conclusions.

CHAPTER 2

EXPERIMENTAL DESIGN AND THEORY

2.1 Jicamarca Radio Observatory Basics

The aspect sensitivity measurements were made at the Jicamarca Radio Observatory (JRO) in Peru (11.95° S, 76.87° W). The main radar at JRO is an incoherent scatter radar (ISR). The radar antenna covers an area approximately 300 m by 300 m and consists of 18,432 half-wave dipoles. The radar has four 1.5 MW transmitters. The main antenna is divided into 64 modules with 144 crossed-dipoles each. The radar beam can be steered up to three degrees off-axis, and when pointed perpendicular to the magnetic field, has a two-way half-power beamwidth of 0.7°. The dip angle over Jicamarca is approximately one-half degree, and Jicamarca's beam can consequently be pointed normal to it.

In addition to the main antenna, the "huayco module" was used in the aspect sensitivity experiment. It is located 391.2 m northwest (aligned with the down polarization of the main array) and 292.6 m northeast (aligned with the up polarization of the main array) of the center of the main array. The huayco module is main up of 4 by 8 Yagis aligned with the down polarization of the main array.

2.2 Interferometry Technique

Since the RMS aspect angles are very small aspect angles being much smaller than the beamwidth of JRO's main array, it is necessary to employ an interferometry technique to measure them. The technique used in this

experiments is based on the one described by *Farley et al.* (1981). The *Farley et al.* (1981) paper further developed a theory originally proposed by *Woodman* (1971) to measure the inclination of the magnetic field.

In radar interferometry, signals are received on two or more spaced antennas. For aspect sensitivity measurements, the receiving antennas are spaced along the geomagnetic field. Other antennas are spaced along the geomagnetic east-west direction to allow for a correction needed due to the baselines not being exactly aligned with the geomagnetic north-south direction. When the signals are received, cross-spectra are formed by cross-correlating the signals. The phase of the cross-spectra gives the bearing of the scatterer in the scattering volume, and the magnitude of the cross-spectra gives the physical extension of the scatterer perpendicular to the magnetic field.

The normalized cross correlation, CC_{12}, between two antennas separated by a physical distance $\mathbf{d}_{12}$ allows for the determination of the angular distribution of arrival angles. Neglecting noise, the normalized cross-correlateion is:

$$CC_{12}(\omega) \equiv \frac{\langle v_1(\omega)^* v_2(\omega)\rangle}{\langle |v_1(\omega)|^2\rangle^{1/2}\langle |v_2(\omega)|^2\rangle^{1/2}} \tag{2.1}$$

$$CC_{12}(\omega) = \langle e^{i\mathbf{k}\cdot\mathbf{d}_{12}}\rangle \tag{2.2}$$

where v_1 and v_2 correspond to frequency domain voltage samples from each antenna and $\mathbf{k}$ is the radar wave vector. Formally, the angle brackets indicate an ensemble average but can be treated as a time average. Since the arrival angles of the scatter are small due to the small aspect angles, equation (2.2) can be expanded as:

$$CC_{12}(\omega) \approx e^{ikd_{12}\langle\phi\rangle}\left(1 - \frac{k^2 d_{12}^2}{2}\left(\langle\phi^2\rangle - \langle\phi\rangle^2\right) + \cdots\right) \tag{2.3}$$

where $\phi \approx \cos(\alpha)$ and α is the mean angle of the scatter with respect to the antenna baseline. Thus, if the baseline were exactly aligned with the

geomagnetic field, $\langle\phi^2\rangle$ would be zero for perfectly field-aligned irregularities. The angular spread of the scatter is of interest, so the phase of the cross-correlation can be ignored. Specifically, the magnitude of the cross-correlations, or coherence, is of interest. The angular distribution of the echoes is defined as and the $\theta_{rms} \equiv \sqrt{\langle\phi^2\rangle - \langle\phi\rangle^2}$.

2.3 Sources of Error

There are four sources of error: statistical error, baseline alignment error, an estimator bias, and mismatched cable lengths. Statistical error and baseline alignment error were explored by *Farley and Hysell* (1996) and the derivation below closely follows the derivation in that work. Bias was not addressed by early work, and a description of the bias correction is included here.

2.3.1 Statistical Errors

The normalized cross-correlation given in equation (2.1) can be rewritten taking into account noise in the received signal:

$$CC_{12}(\omega) = \frac{\langle v_1(\omega)^* v_2(\omega)\rangle}{\langle |v_1|^2 - |v_{1N}|^2\rangle^{1/2}\langle |v_2|^2 - |v_{2N}|^2\rangle^{1/2}} \tag{2.4}$$

where the subscripts v_{1N} and v_{2N} correspond to the noise in receiver 1 and 2 and $\langle v_{1N} v_{2N}^*\rangle = 0$. No noise terms appear in the numerator since the noise should be uncorrelated. Therefore, as given by *Farley and Hysell* (1996) who generalized the method of *Farley* (1969) to include complex samples and correlations, the mean square error for each term is given by:

$$\delta^2 \quad = \quad \langle |\hat{S}_{12} - S_{12}|^2\rangle \tag{2.5}$$

$$\approx \quad \frac{1}{K}\left(\frac{S+N}{S}\right)^2\left[1+\frac{1}{2}|S_{12}|^2\left(1+|\frac{S}{S+N}S_{12}|^2\right)-2\frac{S}{S+N}|S_{12}|^2\right] \tag{2.6}$$

Taking the limit of very high correlations and defining $|S_{12}|^2 = 1-\epsilon$, which together with the limit of $\epsilon << 1$ and assuming $S/N >> 1$, simplifies the mean square error of the cross correlation estimates to:

$$\delta^2 \approx \frac{1}{K}\left[\frac{N}{S}+\frac{1}{2}\epsilon+\vartheta\left(\epsilon^2,\frac{N^2}{S^2},\epsilon\frac{N}{S},\ldots\right)\right] \tag{2.7}$$

which can be small if S/N is large. This means that as S/N increases, the statistical error in the aspect angle measurements decrease, allowing very small angles to be measured. More importantly, as ϵ decreases, the error decreases. Arbitrarily good accuracy is possible as long as the signal-to-noise ratio is high enough.

2.3.2 Baseline Alignment Error

The above derivation assumes all baselines are exactly aligned with the geomagnetic field. However, since there is only a limited number of modules from which to create the antenna baselines, this assumption is not valid. Correcting the baseline alignment error of the cross-correlations is important. If the baseline error is not corrected, the coherence is degraded due to the contribution from the off parallel component.

A baseline vector, $\mathbf{d}_{12}$, can be written as $\mathbf{d}_{12} = (d_x, d_y)$ where d_x is the baseline component perpendicular to the projection of the geomagnetic field onto the ground and d_y is the baseline component parallel to the projection of the geomagnetic field onto the ground. Letting ϕ be the root mean square aspect angle and θ be the misalignment angle, the magnitude of the normalized cross-correlation in equation (2.2) can be written:

$$|CC_{12}| = \langle e^{\frac{i\mathbf{k}\cdot\mathbf{d}_{12}}{2}}\rangle = e^{\frac{-k^2d_x^2\langle\theta^2\rangle}{2}}e^{\frac{-k^2d_y^2\langle\phi^2\rangle}{2}} \tag{2.8}$$

To remove the baseline misalignment error, another baseline is used, **d'**, which is nearly aligned perpendicular to the projection of the geomagnetic field on the ground. The perpendicular baseline, **d'**, can be written as in equation (2.8). Since the baseline is nearly perpendicular to the geomagnetic field, the approximation $e^{\frac{-k^2 d_y^2 \langle \phi^2 \rangle}{2}} \approx 1$ can be made. Thus, the following can be done to remove the baseline alignment error:

$$|CC_{12}| = \frac{e^{\frac{-k^2 d_x^2 \langle \theta^2 \rangle}{2}} e^{\frac{-k^2 d_y^2 \langle \phi^2 \rangle}{2}}}{\left(e^{\frac{-k^2 d_x'^2}{2}}\right)^{\frac{d_x^2}{d_x'^2}}} \tag{2.9}$$

Expanding similarly as in equation (2.3) and solving for the root mean square aspect angle gives:

$$\langle \phi^2 \rangle = (1 - |S_{12}|) \frac{2}{k^2 d_y^2} \tag{2.10}$$

where $k = \frac{2\pi}{\lambda}$ and d_y is the component of the baseline parallel to the projection of the geomagnetic field onto the ground.

2.3.3 Estimator Bias

A bias in the cross-correlation estimate results from the manner in which the expression is normalized. Therefore, when the normalized cross-correlation is very close to unity (as it is for F-region aspect sensitivity measurements) the error cannot deflect the normalized cross-correlation to a value greater than one (*Hysell and Chau*, 2006). Below, the bias is derived, and the correction applied to the normalized cross-correlation is derived.

An estimator for equation (2.1) can be formed as:

$$\hat{CC} = \frac{\frac{1}{m}\sum_{i=1}^{m} v_{1i} v_{2i}^*}{\frac{1}{m}\sum_{i=1}^{m} |v_{1i}|^2 \frac{1}{m}\sum_{i=1}^{m} |v_{2i}|^2} \equiv \frac{A_{12}}{\sqrt{B_{12}}} \tag{2.11}$$

where A_{12} is an unbiased estimator and B_{12} is a biased estimator because of possible correlations in the signals from the two receivers involved. The estimators, A_{12} and B_{12}, deviate from their expectations due to the limited number of samples. Therefore, errors are present in the estimators and are defined as:

$$\begin{aligned} A_{12} &= \langle A_{12} \rangle (1 + \epsilon_{A_{12}}) \\ B_{12} &= \langle B_{12} \rangle (1 + \epsilon_{B_{12}}) \end{aligned} \tag{2.12}$$

where $\epsilon_{A_{12}}$ and $\epsilon_{B_{12}}$ are zero-mean small deviations. The expectations of the estimators are:

$$\langle A_{12} \rangle = \langle \frac{1}{m} \sum_{i=1}^{m} v_{1i} v_{2i}^{*} \rangle = S \cdot CC_{12} \tag{2.13}$$

$$\begin{aligned} \langle B_{12} \rangle &= \langle \frac{1}{m} \sum_{i=1}^{m} |v_{1i}|^2 \frac{1}{m} \sum_{i=1}^{m} |v_{2i}|^2 \rangle \\ &= \frac{1}{m} \left(1 + |CC_{12}|^2 \right) S^2 + \frac{m(m-1)}{m^2} S^2 \\ &= S^2 \left(1 + \frac{1}{m} |CC_{12}|^2 \right) \end{aligned} \tag{2.14}$$

where S is the signal power. The second term in the final line of equation (2.14) is the bias due to correlation between the two receiver channels. Therefore, to correct for bias the following is used:

$$|C\hat{C}'_{12}| = |C\hat{C}_{12}| \left(1 + \frac{1}{2} \frac{|C\hat{C}_{12}|^2}{m} \right) \tag{2.15}$$

where $|C\hat{C}'_{12}|$ is the corrected coherence and $|CC|$ is the uncorrected coherence.

2.3.4 Mismatched Cable Length

The cable lengths at Jicamarca are not all identical. A correction to the arrival time of the data needs to be made so the data being cross-correlated is from the

same sample range. This correction was only applied to the data received on the huayco module. The other modules did not have the correction made, but the mismatches in cable length are relatively small. Thus, the mismatch in cable length likely has degraded the coherences slightly, but because the integration time for the measurements was fairly long, the errors introduced from correlation samples collected at two different times is negligible.

The mismatch in cable length for the huayco module was corrected as follows. A block of complex voltage data from the huayco module is appended with an equal number of zeros. It is inverse Fourier transformed into the frequency domain:

$$v_h(\omega) = \mathscr{F}^{-1}[v_h(t)] \tag{2.16}$$

where $v_h(t)$ is the time domain voltage from the huayco receiver and $v_h(\omega)$ is the frequency domain voltage. The correct phase shift is applied to offset the phase shift imposed by the cable length mismatch:

$$v'_h(\omega) = v'_h(\omega)\,(\cos\alpha + i\sin\alpha) \tag{2.17}$$

where $v'_h(\omega)$ is the frequency domain voltages corrected for the phase delay, α. The phase delay correction is dependent on frequency. The corrected complex data data is then Fourier transformed back into the time domain:

$$v'_h(t) = \mathscr{F}[v'_h(\omega)] \tag{2.18}$$

The data is then treated the same as the other data.

2.4 Setup of the March 1993 Experiment

The first F-region aspect sensitivity measurements were made in March 1993 using the JRO main radar (*Farley and Hysell*, 1996; *Hysell and Farley*, 1996). For

this experiment, *Farley and Hysell* (1996) transmitted using the east and west quarters of the antenna and received on only four channels (the two quarters used to transmit and two of the 64 modules). The antenna configuration is shown in Figure 2.1.

Since analog recievers were being used for the March, 1993 experiments the setup had to consider the potential nonlinear effects introduced. To try and account for these errors, the output from the front-end *D* (Figure 2.1) is fed into a power splitter, with half of the power going to a switch and the remainder going to the receiver *D*. At every pulse, the switch toggles so that half of the time the signal from the *D* front-end is fed into receiver *B*. This allows for reciever *B* and reciever *D* to have the same input (ideally the switch would be in front of the receiver front-ends). By having identical signals fed into the receivers, it was possible to calibrate for the effects from analog receivers. The JRO system has been upgraded to all digital receivers by the March, 2009 experiments. Therefore, this calibration is no longer neccesary.

2.5 Setup of the March 2009 Experiment

The data presented were collected on the evening of March 18, 2009. The antenna configuration for this experiment is shown in Figure 2.2. The antenna configuration differs from that of 1993 by using eight modules (including the huayaco module) to receive. As in the 1993 experiment, the east and west antenna quarters were used to transmit. The addition of the huayco also doubled the longest baseline available. Frequency multiplexing was used to for the inputs into the receivers. Modules A, C, E, and F were fed into the 50 MHz inputs allowing for the highest coherence and the others were fed into the 42.5 MHz inputs. Frequency multiplexing is neccesary as there are only

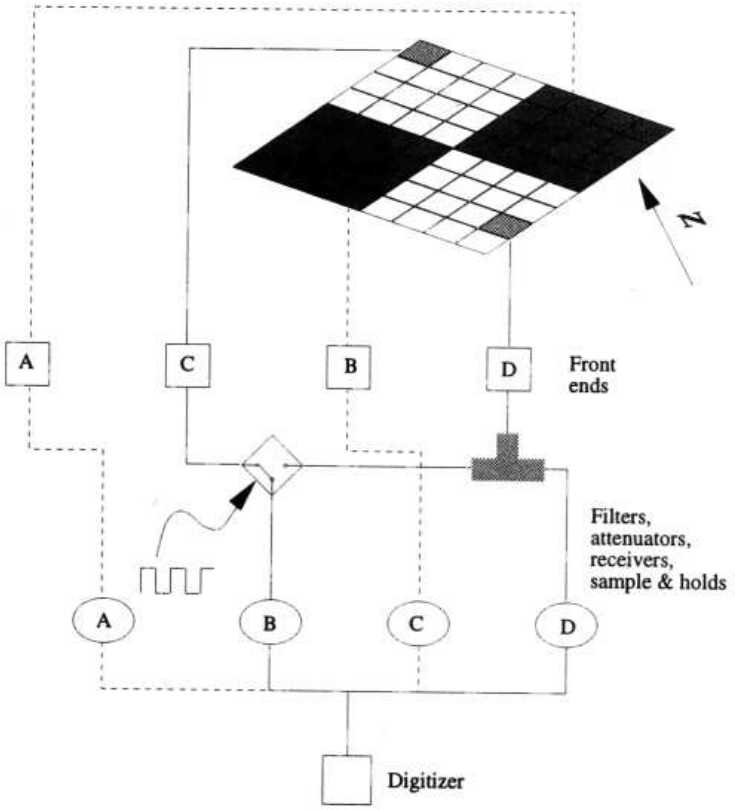

Figure 2.1: The antenna configuration used in the March 1993 F-region aspect sensitivity experiment. (After *Farley and Hysell* (1996).)

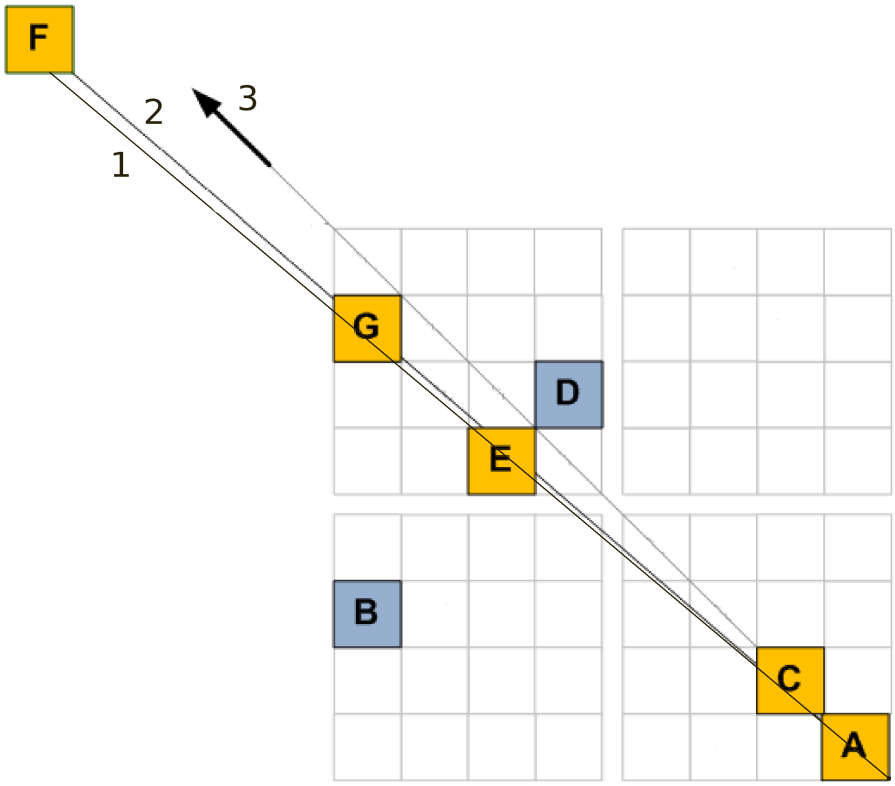

Figure 2.2: Schematic of the March, 2009 experiment. *Line* 1 is the geomagnetic north-south direction ($d_{\parallel}$). *Line* 2 is the A-F baseline. *Line* 3 is the alignment of the JRO main antenna which was parallel to the geomagnetic north-south when first constructed. Each module labeled A-F is a module used to receive and corresponds to the labels in Table 2.4. The orange modules are primarily along the north-south baselines and the blue modules are primarily along the east-west baselines.

Table 2.1: The misalignment angle from parallel to the projection of the geomagnetic field of the baselines and the projection of the baseline onto the parallel and perpendicular components of the magnetic field.

Baseline Pair	Misalignment Angle (deg)	$d_{\parallel}$ (in λ)	$d_{\perp}$ (in λ)
A-F	0.703	111.237	1.365
C-F	0.209	102.809	0.375
E-F	0.827	72.116	1.041
A-G	2.357	55.975	2.304
F-G	-0.973	55.262	-0.939
C-G	1.583	47.548	1.314
A-E	0.474	39.120	0.324
C-E	-1.243	30.693	-0.666
E-G	6.700	16.855	1.980
A-C	6.700	8.427	0.990
B-D	82.515	3.362	25.592
B-E	83.300	1.980	16.855
D-E	83.300	0.990	8.427

four recievers with two inputs each. The main transmitters were used for the experiment. The sampling interval was $2\mu s$ and the pulse width was $4\mu s$. Ranges were sampled from 90 km to 600 km with range resolution of 300 m.

Despite the improvements from the 1993 experiment, several new issues were introduced. The high sampling rate caused data to occasionally not be recorded. To account for this, care was taken to examine intervals with a constant time step. Also, although the receivers are now digital, they still have an analog mixer on the front end for frequency multiplexing to allow all receiver inputs to be used.

CHAPTER 3

DATA PRESENTATION

3.1 Data from March 1993

To provide context to the 2009 measurements, the results of the 1993 experiment by Farley and Hysell [1996] are presented (*Farley and Hysell*, 1996; *Hysell and Farley*, 1996).

Figures 3.1 and 3.2 show the results from scatter from ESF during the 1993 experiment. The main results of the experiment were (*Farley and Hysell*, 1996; *Hysell and Farley*, 1996):

1. Full aspect angle (two times RMS aspect angle) spreads of bottomside irregularities are less than 0.03° from perfect alignment.
2. The aspect angle is independent of Doppler frequency.
3. The aspect angle is nearly the same in both bottomside and topside ESF layers.

3.2 Data from March 18, 2009

Data were collected from from 1930 LT until 2200 LT on March 18, 2009. There were periodic data gaps in addition to the data dropouts mentioned in the previous chapter. The experimental parameters were presented previously. March 18 was a geomagnetically quiet day with Kp < 2. For the present study, all aspect angles are presented using the RMS aspect angle. *Farley and Hysell* (1996) and *Hysell and Farley* (1996) presented their data using the "full" aspect angle, or 2ϕ RMS, in presenting their data whereas this study presents the data

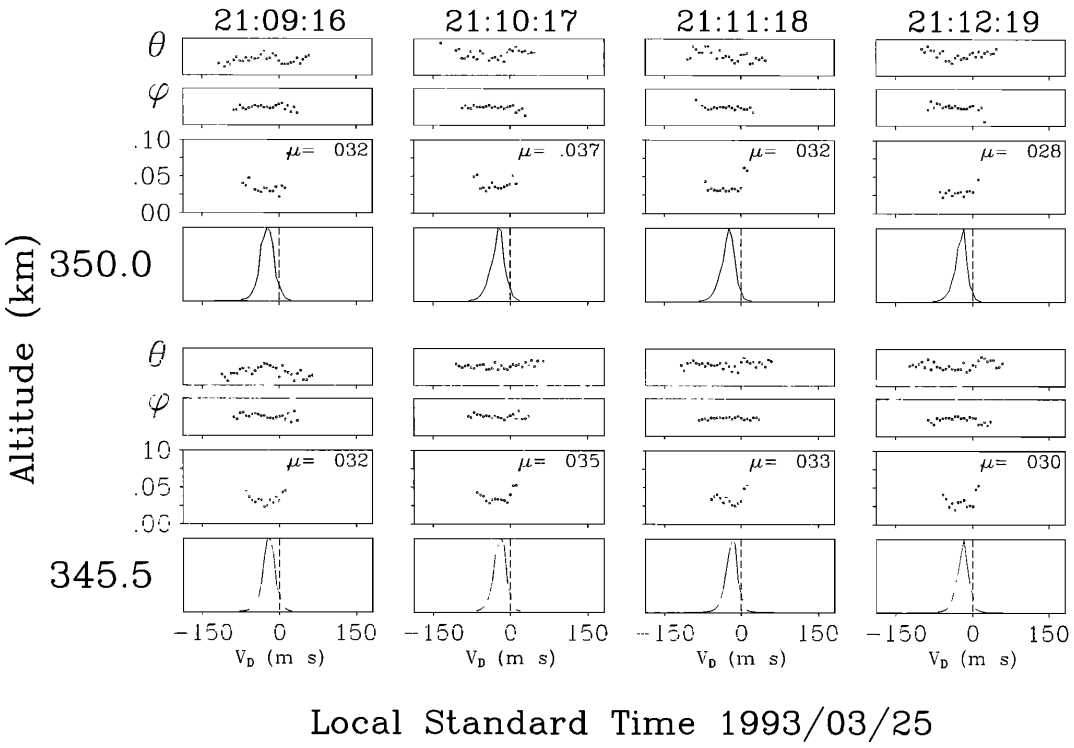

Figure 3.1: Data from a bottomside spread-F layer. From top to bottom the panels show the power spectrum, the full aspect width (2 times RMS aspect angle) in degrees with the mean value of the stronger signals shown in the corner, the relative mean position for each Doppler bin in the magnetic meridian plane, and the relative mean position for each Doppler bin in the east-west plane. (After *Farley and Hysell* (1996).)

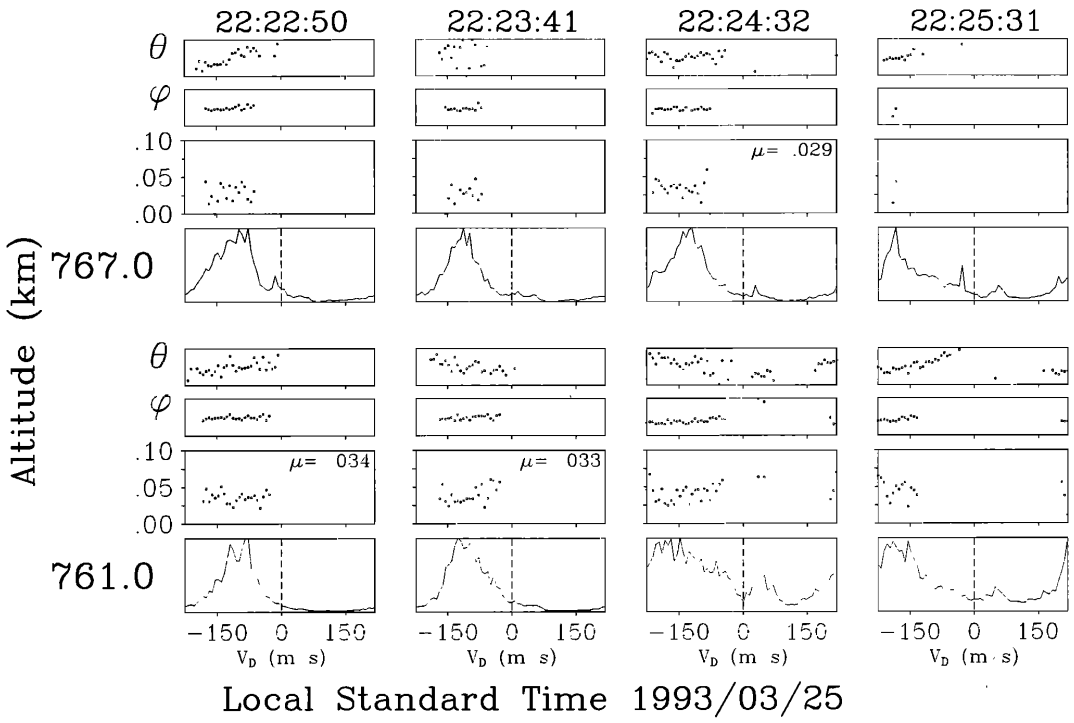

Figure 3.2: The figure shows data in the same manner as Figure 3.1 but for topside ESF. (After *Farley and Hysell* (1996))

using the RMS aspect angle, or ϕ. Therefore, to compare data between the 1993 and the 2009 experiments, a factor of 2 must be applied.

The RTI plot of the signal for March 18 is shown in Figure 3.3. It can be seen that a large plume developed shortly before 2130 LT and reached heights of over 500 km. By 2215 LT the only ESF still present was a thin layer of bottomside ESF. Figure 3.4 shows an RTI plot of the aspect angle for the A–F baseline after 2045 LT. The aspect angle does not have any universal correlation to the magnitude of the signal. Inside the plume the aspect angle ranges from .0025°–.01°. Figure 3.5 shows the error in the aspect angles presented in Figure 3.4. The error is seen to decrease mildly as the aspect angle decreases, with a value of 0.001°–0.0025° inside the plume. Therefore, the RMS aspect

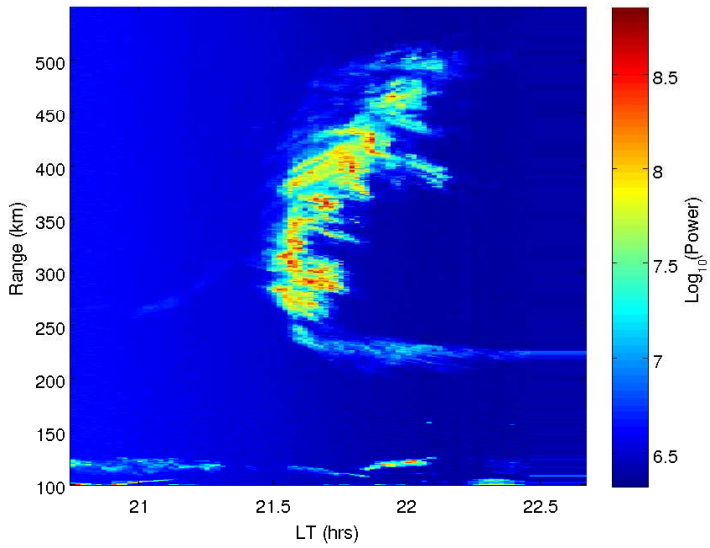

Figure 3.3: A RTI of the $\log_{10}$ of the signal from the A–F baseline for the zero-frequency bin.

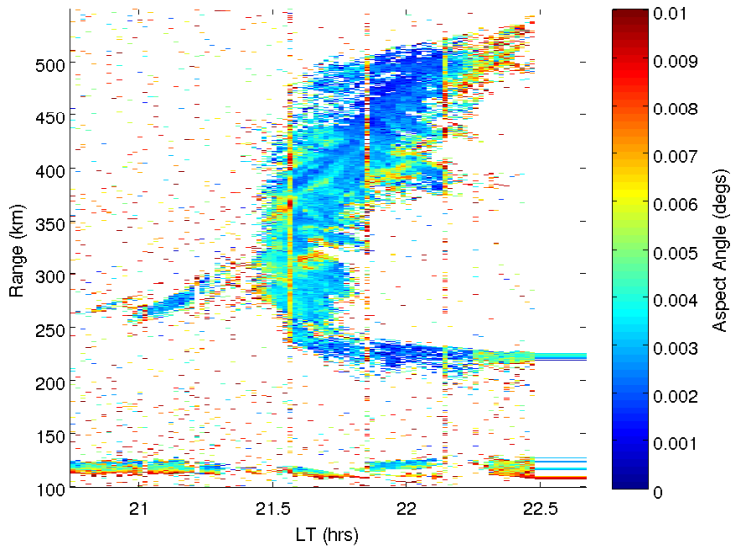

Figure 3.4: A RTI of the RMS aspect angle based on the A–F baseline for the zero-frequency bin on the evening of March 18, 2009.

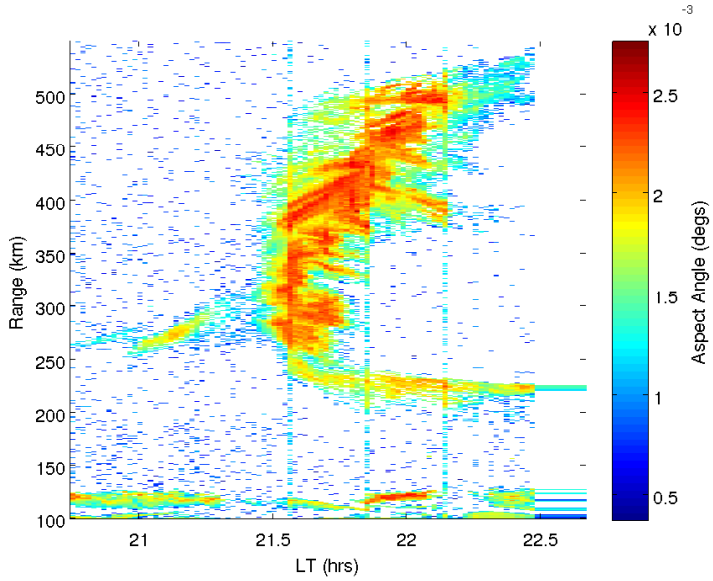

Figure 3.5: A RTI of the error in RMS aspect angle based on the A-F baseline for the zero-frequency bin on the evening of March 18, 2009.

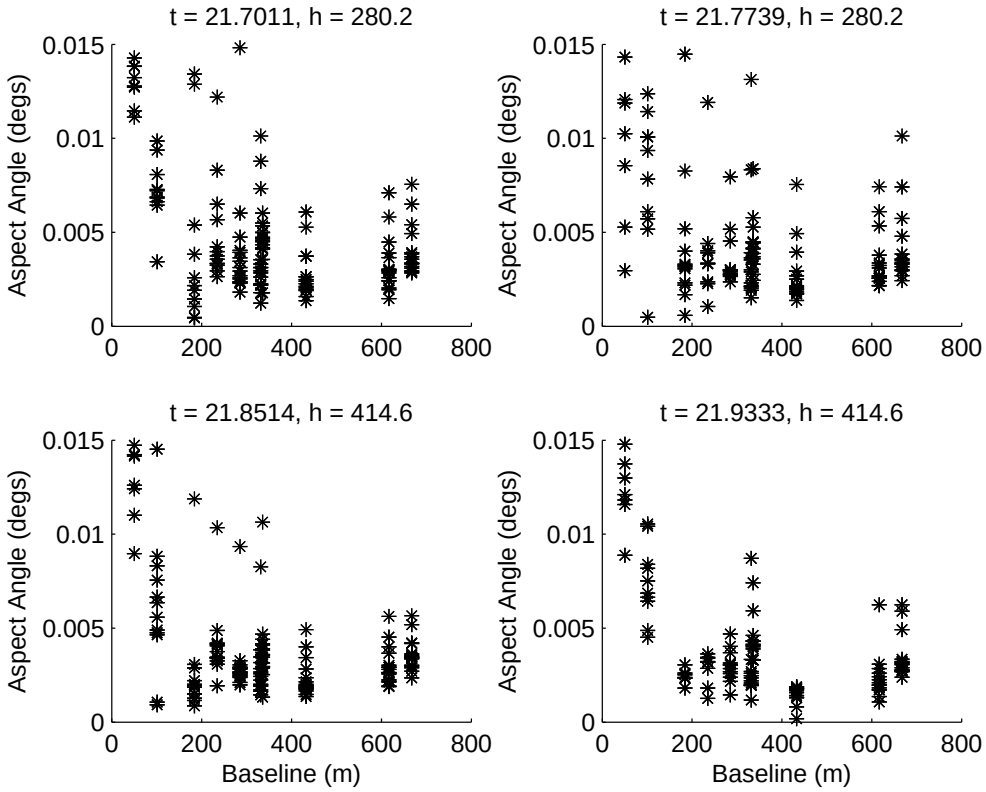

Figure 3.6: RMS aspect angle plotted against baseline length at four different times and two different heights on March 18, 2009 for all Doppler bins.

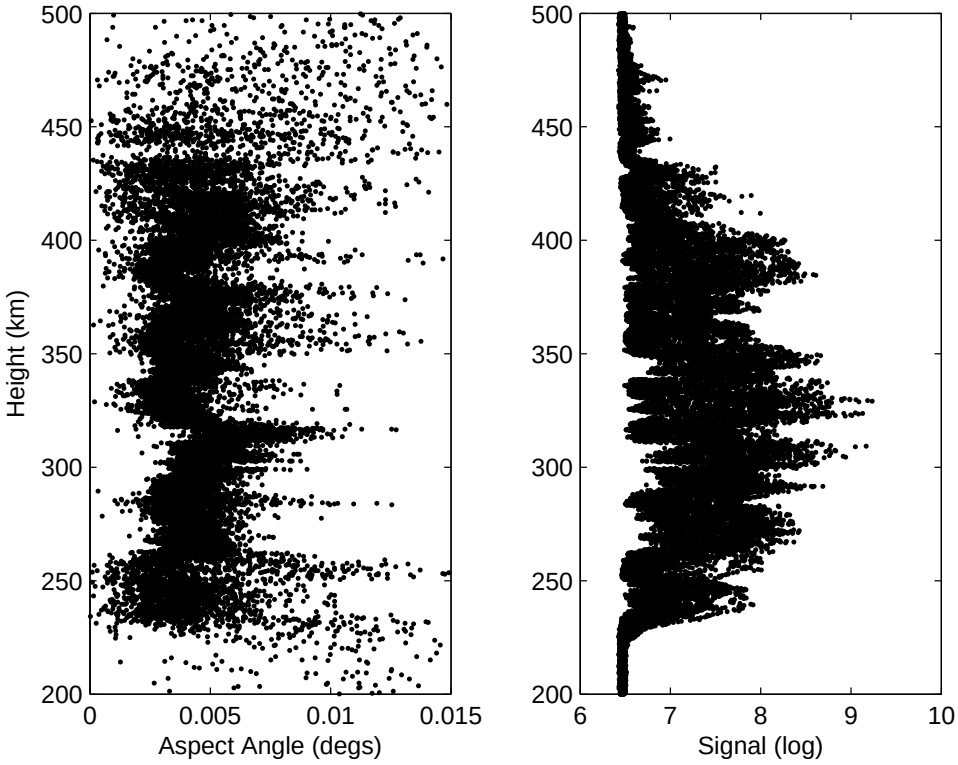

Figure 3.7: Left: RMS aspect angle plotted against height for the A–F baseline at 2142 LT with all Doppler bins included. Right: Signal plotted against height for the A–F baseline at 2142 LT with all Doppler bins included.

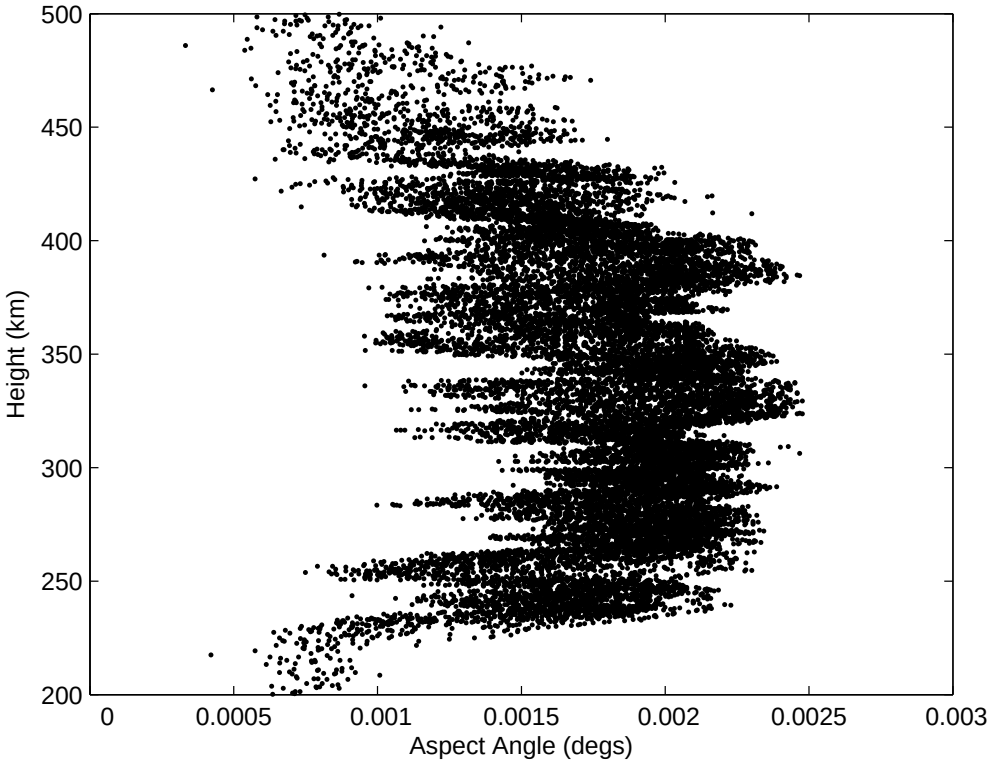

Figure 3.8: Error in the RMS aspect angle plotted against height for the A–F baseline and a single time with all Doppler bins included.

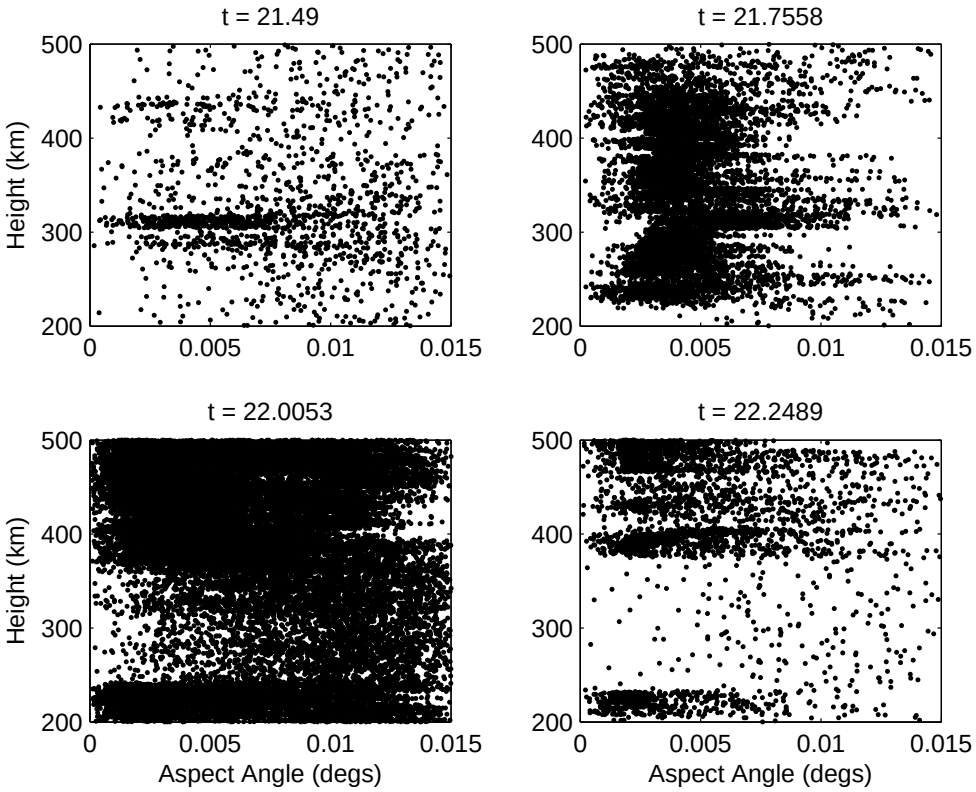

Figure 3.9: RMS aspect angle from the A–F baseline plotted against height for four times with all Doppler bins included.

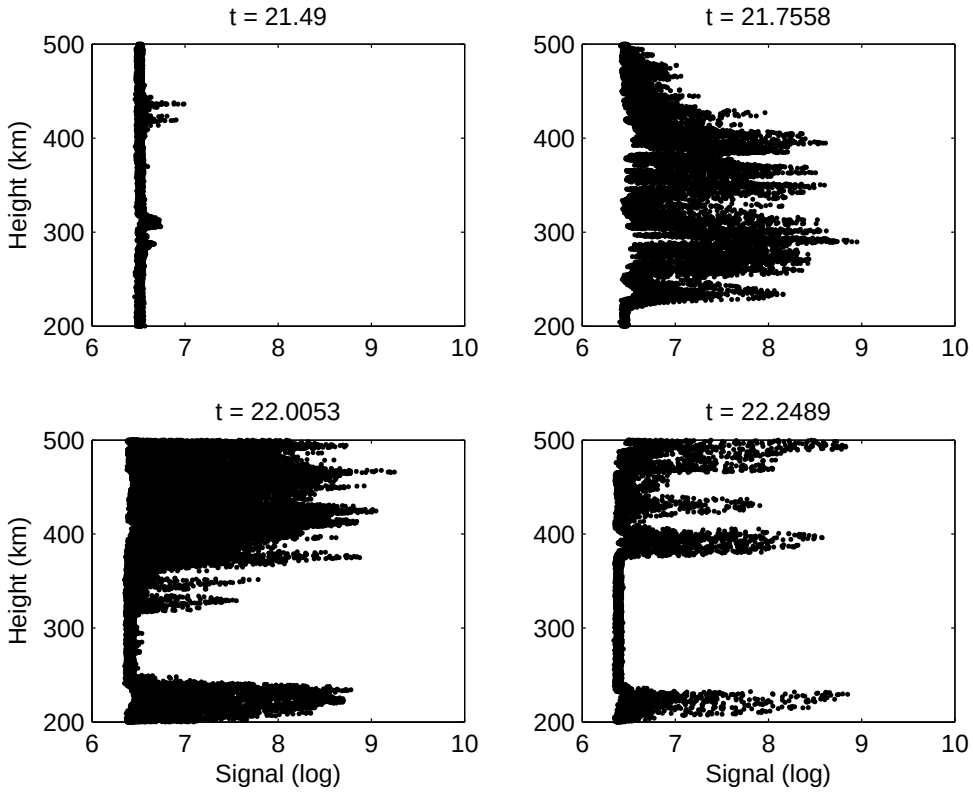

Figure 3.10: Signal from the A–F baseline plotted against height for four times with all Doppler bins included.

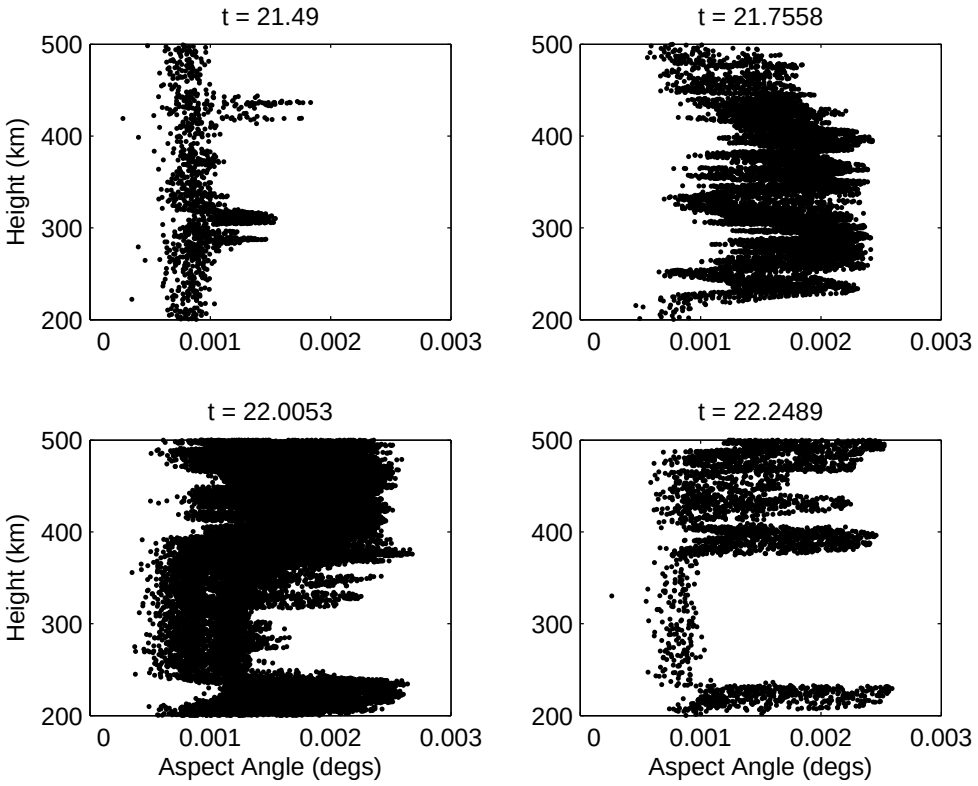

Figure 3.11: Error in the RMS aspect angle from the A–F baseline plotted against height for four times with all Doppler bins included.

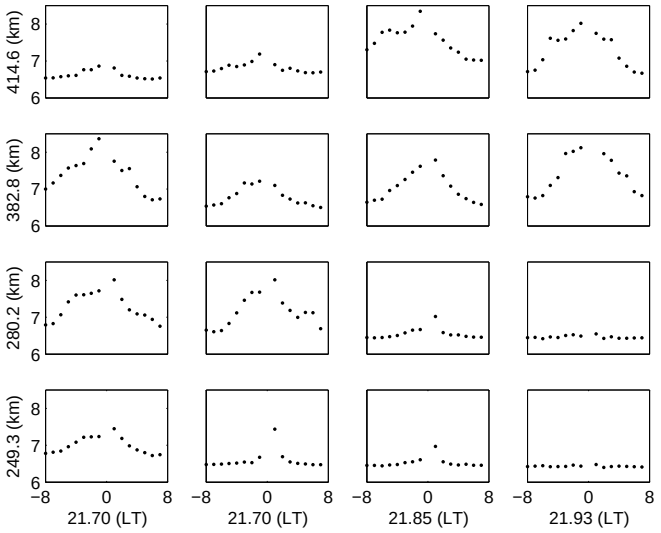

(a)

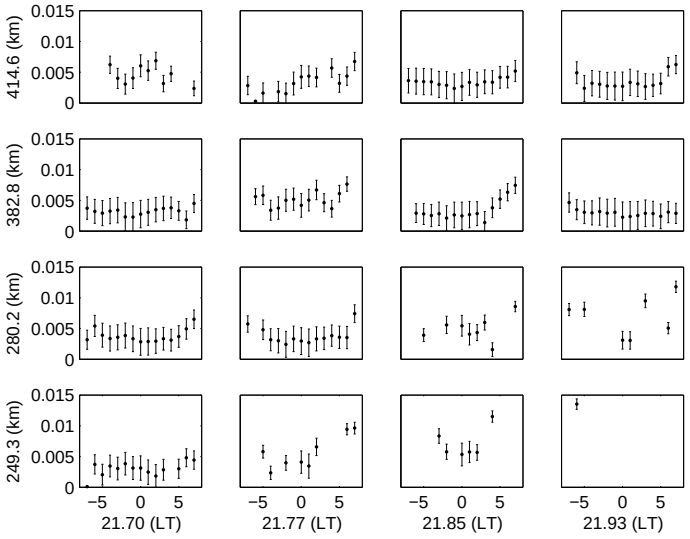

(b)

Figure 3.12: Figure 3.12(a) shows the power spectra for the times and heights shown. Figure 3.12(b) shows the RMS aspect angle plotted against frequency bin (the zero-frequency bin is corresponds to zero in the plots).

angles are uniformly larger than their errors.

Of particular interest during the March, 2009 experiment was how dependent the aspect angle was on the length of the baseline. Figure 3.6 shows the aspect angle plotted against baseline length for four different times, two different altitudes, and all Doppler bins. It is evident that, after the two shortest baselines, the aspect angle does not have a dependence on the baseline length. It is likely that the two shortest baselines are so short that the interferometry technique fails.

To illustrate the point of the interferometry technique failing we examine the case of the shortest baseline (the A-C baseline). The mean squared error is given in equation (2.7), and for the shortest baseline typical values where $K \approx 1500$, $\frac{N}{S} \approx .05$, $\epsilon \approx .02$. This gives an error in the coherence of 4×10^{-5}, so the most accurate coherence can be measured to is .9999. A coherence of .9999 corresponds to an RMS aspect angle in degrees of .015° which is greater than the the angles typically measured. Thus, for the shortest baselines the challenge of differentiating between coherences very nearly unity and those very, very near unity becomes intractible.

Figure 3.7 plots the aspect angle as a function of height for all Doppler bins at 2142 LT for the A–F baseline and the corresponding signal; Figure 3.8 plots the corresponding errors. Additionally, Figure 3.9 plots four additional times of aspect angle as a function of height for all Doppler bins and Figure 3.10 plots the corresponding signal; Figure 3.11 plots the corresponding errors. The aspect angle does not exhibit a height dependence. The majority of the time, but not universally, as the signal increases the spread and magnitude of the aspect angle decreases. Also, as mentioned above, the error in the aspect angle increases marginally as the aspect angle decreases.

Figure 3.12(a) presents the power spectra for four heights and times. The corresponding aspect angle spectra are presented in Figure 3.12(b). The power spectra are well behaved, and the aspect angle spectra show no dependence of aspect angle with Doppler frequency or on height. The lack of dependence on Doppler bin indicates the interferometry technique is working. Frames that are missing some aspect angle values were in regions of low density and coherence (for the case of 21.93 LT, the bottomside of the plume was at approximately 280-km; also see Figure 3.12(a)) where the interferometry technique failed. The spectra exhibit normal variation mostly within their error bars.

CHAPTER 4

CONCLUSIONS

The aspect sensitivity measurements of March, 2009 confirmed the early findings from March, 1993. Additionally, due to using digital receivers it was possible to greatly reduce the magnitude of the errors and determine an absolute measure of the aspect angle. In particular, for F-region irregularities, the mean aspect angle is found to be less than .01° the majority of the time (corresponding to a "full" aspect angle of .02°). However, the upper limit of .015° RMS aspect angle found is consistent with the upper limit of the 1993 experiment.

As in *Farley and Hysell* (1996) and *Hysell and Farley* (1996), it is found that the aspect angle is independent of Doppler velocity and height. Further, the aspect angle is found to have no dependence on height within a plume. However, there is structure seen with altitude within the plume, but it is not a general increasing or decreasing trend. This structure is unexpected, and is likely explained by areas of newer (older) irregularites causing an increase (decrease) in the aspect angle. The explanation of the structure as corresponding to areas of newer or older irregularities, would be further supported if the aspect angle increased (decreased) as signal power increased (decreased). However, no general correlation between signal power and aspect angle is seen. Thus, the findings of the present study tentatively support the theory presented in *Hysell and Farley* (1996)

The present study examined the dependence of the aspect angle on baseline length. No dependence was found, indicating the distribution of aspect angles is in fact a Gaussian distribution. In making this conclusion the shortest two baselines are ignored, and the increased frequency spread of the

two shortest baselines indicate the interferometry method is failing. As seen in the previous chapter, the failure of the shortest two baselines is not surprising. For short baselines the coherences become so small that they are overwhelmed by error and noise.

Several new sources of error and corrections were introduced in this study. In particular, the correction method for the baseline misalignment error has not been applied to any previous aspect sensitivity measurements in either the E-region or F-region. Also, the bias correction was not employed in the 1993 study. The implimentation of these new corrections, along with increased baselines and improved receivers, has allowed for the present study to acheive greater accurracy.

Despite making a significant improvement from the 1993 experiment in aspect sensitivity measurements, several issues remain. As discussed earlier, not all mismatches in cable length were accounted for, but the error introduced is expected to be negligible. Additionally, the sampling rate was high enough that data was lost even though a high sampling rate is not required. In future studies care needs to be taken to ensure experimental parameters are well within the capabilities of the data aquisition system.

With the new method for correcting baseline alignment error it is important to choose east-west baselines that are closest to the projection of the north-south baselines onto the geomagnetic east-west ($d_x \approx d'_x$). Finally, the receiver system at Jicamarca is not entirely digital yet, and therefore some non-linear effects are introduced. Thus, a calibration similar to that of the 1993 experiment should be done to provide a calibration.

In this study, at smaller aspect angles the magnitude of the errors approached the magnitude of the aspect angles. Therefore, it is not possible to

say with certainty what the aspect angle of F-region plasma instabilities is. However, it is shown the aspect angle is measurable to within a few thousandths of a degree. Thus, future studies need to be mindful of the preventable shortcomings of the current and previous studies in order to acheive the required sensitivity to measure absolute aspect angles.

BIBLIOGRAPHY

Berkner, L. V., and H. W. Wells (1934), F-region ionosphere investigation at low altitudes, *Terr. Magn.*, *39*, 215.

Farley, D. T. (1969), Incoherent scatter correlation function measurements, *Radio Sci.*, *4*, 935.

Farley, D. T., and D. L. Hysell (1996), Radar measurement of very small aspect angles in the equatorial ionosphere, *J. Geophys. Res.*, *101*, 5177.

Farley, D. T., B. B. Balsley, R. F. Woodman, and J. P. McClure (1970), Equatorial spread F: Implications of VHF radar observations, *J. Geophys. Res.*, *75*, 7199.

Farley, D. T., H. M. Ierkic, and B. G. Fejer (1981), Radar interferometry: A new technique for studying plasma turbulence in the ionosphere, *J. Geophys. Res.*, *86*, 1467.

Hysell, D. L., and D. T. Farley (1996), Implications of the small aspect angles of equatorial spread F, *J. Geophys. Res.*, *101*, 5165.

Hysell, D. T., and J. L. Chau (2006), Optimal aperture synthesis radar imaging, *Radio Sci.*, *41*.

Kelley, M. C. (2009), *The Earth's Ionosphere*, Second Edition ed., Academic Press.

Kudeki, E., and D. Farley (1989), Aspect sensitivity of equatorial electrojet irregularities and theoretical implications, *J. Geophys. Res.*, *94*, 426.

Woodman, R. F. (1971), Inclination of the geomagnetic field measured by an incoherent scatter technique, *J. Geophys. Res.*, *76*, 178.